JGR Atmospheres

RESEARCH ARTICLE
10.1029/2020JD034523

Transport of Nitric Oxide Via Lagrangian Coherent Structures Into the Top of the Polar Vortex

V. Lynn Harvey[1,2], Seebany Datta-Barua[3], Nicholas M. Pedatella[4], Ningchao Wang[5], Cora E. Randall[1,2], David E. Siskind[6], and Willem E. van Caspel[7,8]

[1]Laboratory for Atmospheric and Space Physics, University of Colorado, Boulder, CO, USA, [2]Department of Atmospheric and Oceanic Sciences, University of Colorado, Boulder, CO, USA, [3]Department of Mechanical, Materials, and Aerospace Engineering, Illinois Institute of Technology, Chicago, IL, USA, [4]High Altitude Observatory, National Center for Atmospheric Research, Boulder, CO, USA, [5]Department of Atmospheric Sciences, Hampton University, Hampton, VA, USA, [6]Space Science Division, Naval Research Laboratory, Washington, DC, USA, [7]Department of Physics, Norwegian University of Science and Technology, Norway, [8]Birkeland Centre for Space Science, University of Bergen, Bergen, Norway

Abstract The energetic particle precipitation (EPP) indirect effect (IE) refers to the downward transport of reactive odd nitrogen (NO_x = NO + NO_2) produced by EPP (EPP-NO_x) from the polar winter mesosphere and lower thermosphere to the stratosphere where it can destroy ozone. Previous studies of the EPP IE examined NO_x descent averaged over the polar region, but the work presented here considers longitudinal variations. We report that the January 2009 split Arctic vortex in the stratosphere left an imprint on the distribution of NO near the mesopause, and that the magnitude of EPP-NO_x descent in the upper mesosphere depends strongly on the planetary wave (PW) phase. We focus on an 11-day case study in late January immediately following the 2009 sudden stratospheric warming during which regional-scale Lagrangian coherent structures (LCSs) formed atop the strengthening mesospheric vortex. The LCSs emerged over the north Atlantic in the vicinity of the trough of a 10-day westward traveling planetary wave. Over the next week, the LCSs acted to confine NO-rich air to polar latitudes, effectively prolonging its lifetime as it descended into the top of the polar vortex. Both a whole atmosphere data assimilation model and satellite observations show that the PW trough remained coincident in space and time with the NO-rich air as both migrated westward over the Canadian Arctic. Estimates of descent rates indicate five times stronger descent inside the PW trough compared to other longitudes. This case serves to set the stage for future climatological analysis of NO transport via LCSs.

Plain Language Summary Energetic particles from the sun and the magnetosphere impinge upon Earth's upper atmosphere and create reactive odd nitrogen (NOx) in the mesosphere and lower thermosphere. Descent in the winter polar vortex effectively transports this NOx down to the stratosphere where it can destroy ozone. State-of-the-art models currently underestimate this vertical transport by a factor of 4. Previous studies have examined the NOx descent averaged over the entire polar region, but this study considers longitudinal variations. We examine a case study during late January 2009 and find a closed circulation coincident with the trough of a planetary wave over the north Atlantic at 90 km with shear zones inhibiting horizontal mixing to the north, east, and south. This circulation (1) contains elevated NOx, (2) is associated with five times stronger descent compared to other longitudes, and (3) is the natural upward continuation of the westward tilting polar vortex in the stratosphere and mesosphere. Thus, this meteorological feature near the mesopause provides a transport pathway for air to enter the top of the polar vortex. This is the first work to illustrate the zonally asymmetric nature of NOx descent in the polar winter upper mesosphere and couple it to the vortex below.

Key Points:

- First demonstration of the impact of the split Arctic vortex on the geographic distribution of nitric oxide at the winter mesopause
- First evidence that a Lagrangian coherent structure inhibits horizontal transport of nitric oxide at the polar winter mesopause
- Descent of nitric oxide is five times stronger between 80 and 90 km in a westward traveling planetary wave trough compared to the ridge

Correspondence to:
V. L. Harvey,
lynn.harvey@lasp.colorado.edu

Citation:
Harvey, V. L., Datta-Barua, S., Pedatella, N. M., Wang, N., Randall, C. E., Siskind, D. E., & van Caspel, W. E. (2021). Transport of nitric oxide via Lagrangian coherent structures into the top of the polar vortex. *Journal of Geophysical Research: Atmospheres*, *126*, e2020JD034523. https://doi.org/10.1029/2020JD034523

Received 31 DEC 2020
Accepted 5 MAY 2021

Author Contributions:

Conceptualization: V. Lynn Harvey
Data curation: V. Lynn Harvey, Willem E. van Caspel
Formal analysis: V. Lynn Harvey, Seebany Datta-Barua, Nicholas M. Pedatella, Ningchao Wang, Willem E. van Caspel
Funding acquisition: V. Lynn Harvey
Investigation: V. Lynn Harvey, Nicholas M. Pedatella, Ningchao Wang
Methodology: V. Lynn Harvey, Seebany Datta-Barua, Nicholas M. Pedatella
Project Administration: V. Lynn Harvey

1. Introduction

The winter polar vortex plays a key role in controlling the atmospheric response to energetic particle precipitation (EPP). In particular, the polar vortex modulates the EPP Indirect Effect (EPP IE), defined as descent to the stratosphere of reactive odd nitrogen (NO_x = NO + NO_2) produced by EPP (EPP-NO_x) (Randall et al., 2006, 2007). Downward transport of EPP-NO_x from the thermosphere into the mesosphere occurs mainly via rapid eddy and molecular diffusion (Garcia et al., 2007; Meraner & Schmidt, 2016; Smith

Resources: V. Lynn Harvey, Nicholas M. Pedatella
Software: V. Lynn Harvey, Seebany Datta-Barua, Ningchao Wang
Supervision: V. Lynn Harvey
Validation: V. Lynn Harvey
Visualization: V. Lynn Harvey, Seebany Datta-Barua, Ningchao Wang, Willem E. van Caspel
Writing – original draft: V. Lynn Harvey
Writing – review & editing: V. Lynn Harvey, Seebany Datta-Barua, Nicholas M. Pedatella, Ningchao Wang, Cora E. Randall, David E. Siskind, Willem E. van Caspel

et al., 2011; Smith, 2012). Below the mesopause, air gets swept into the global wave-driven residual circulation (Andrews et al., 1987), which is characterized by rising motion over the summer pole, strong cross-equatorial flow from the summer hemisphere to the winter hemisphere, and descent in the winter polar vortices (Fisher et al., 1993; Kvissel et al., 2012; Manney et al., 1994; Rosenfield et al., 1994; Schoeberl et al., 1992). In the lower mesosphere and stratosphere, NO reacts with ozone, maintaining an equilibrium with NO_2 via the NO_x catalytic cycle (e.g., Garcia & Solomon, 1994). Thus, any excess stratospheric NO_x from the EPP IE has the potential to impact ozone distributions and thus net radiative heating rates, temperatures, winds, and wave filtering (e.g., Baumgaertner et al., 2011; Sinnhuber et al., 2018).

The EPP IE is especially pronounced following prolonged sudden stratospheric warmings (SSWs) (e.g., Limpasuvan et al., 2016; McLandress et al., 2013; Siskind et al., 2010) when strong mesospheric descent transports unusually large amounts of EPP-NO_x down to the polar stratosphere. SSWs are dramatic wintertime dynamical events, driven by upward propagating planetary waves, that result in a warming of the polar stratosphere, a reversal of the westerly polar night jet stream, and a displaced or split polar vortex (Baldwin et al., 2020; Butler et al., 2017; Scherhag, 1952). While many studies have used zonal averages to show the descent of EPP-NO_x (e.g., Bailey et al., 2014; Hauchecorne et al., 2007; Natarajan et al., 2004; Paivarinta et al., 2016; Pérot et al., 2014; Pérot & Orsolini, 2021; Randall et al., 1998, 2006, 2007, 2009; Reddmann et al., 2010; Rinsland et al., 2005; Siskind et al., 1997, 2000), only a few have shown how the NO_x distribution depends on latitude and longitude (Randall et al., 2005; Salmi et al., 2011; Siskind et al., 2021); and none have shown how NO_x descent varies in space and time. This work fills this gap by analyzing zonal asymmetries in nitric oxide (NO, the primary constituent of NO_x at mesosphere and lower thermosphere (MLT) altitudes), and by quantifying the dependence of NO descent on both latitude and longitude.

Salmi et al. (2011) showed polar maps of enhanced NO_x near 50, 60, and 70 km in February and March following the 2009 SSW, which suggested that zonal averaging could be appropriate to delineate the region of elevated NO_x at those altitudes. However, Newnham et al. (2020) compared zonal asymmetries in Solar Occultation For Ice Experiment (SOFIE) NO from 70-90 km during 17 geomagnetic storms from 2008–2014 to the climatologically preferred longitude sector of the mesospheric polar vortex (Harvey et al., 2018) and hypothesized enhanced vertical coupling when the two are in-phase. Indeed, climatologically, maximum observed electron fluxes occur over the Scandinavian longitude sector (Newnham et al., 2020) and the mesospheric polar vortex is present most often in the longitude sector over nearby Greenland (Harvey et al., 2018), suggesting an in-phase relationship between the two is common. This is consistent with maximum mesospheric descent rates being displaced toward northern Greenland following the 2004 SSW (Winick et al., 2009). Recent analysis of three-dimensional descent also confirms the highest NO concentrations near 300°E longitude following the 2013 SSW (Siskind et al., 2021). In contrast to Salmi et al. (2011), results presented here confirm that zonally asymmetric vertical coupling occurred at an altitude higher than their analysis, near the mesopause, following the 2009 SSW. This work identifies a region of enhanced NO and strong descent at the mesopause over the north Atlantic and Canadian Arctic in the wake of the SSW and shows that this region is located directly above the reforming mesospheric polar vortex.

At MLT altitudes (60–110 km) EPP-NO_x consists primarily of NO, which is initially distributed over a range of geomagnetic latitudes that span auroral and subauroral regions. A notable distinction exists between NO created inside versus outside the polar night. In sunlight at MLT altitudes, NO has a chemical lifetime of several days, whereas in the polar night NO may persist for weeks or months (Bender et al., 2019; Brasseur & Solomon, 2005; Minschwaner & Siskind, 1993). In theory, NO that remains confined to polar darkness, where its lifetime is long, may descend to the stratosphere while NO that is transported to sunlit latitudes will be destroyed. It is therefore of primary interest to identify mechanisms that act to confine NO to high latitudes in winter. Motivated by Sun-Earth coupling via the EPP IE, and by the fact that models underestimate the EPP IE (Funke et al., 2017; Meraner et al., 2016; Orsolini et al., 2017; Pettit et al., 2019; Randall et al., 2015; Sheese et al., 2013; Sinnhuber et al., 2018; Smith-Johnsen et al., 2018), this work examines the effect of Lagrangian coherent structures (LCSs) on the transport of NO in the polar winter MLT. We hypothesize that confinement of NO to high latitudes by LCSs effectively increases the NO lifetime and facilitates NO transport into the top of the polar vortex. Since descent occurs in three dimensions (Callaghan & Salby, 2002; Demirhan Bari et al., 2013; Kinoshita et al., 2010), longitudinal variability can be highly relevant, and this is assessed in our analysis.

LCSs are transport barriers that define different characteristic regions of a flow; they are objective and quantifiable as surfaces of maximum finite-time Lyapunov exponent (FTLE) (Haller, 2015). The FTLE is a scalar field that measures the degree of stretching after a given interval of time of a fluid particle at a certain point, relative to its initial extent. The basic equations may be found in numerous resources (e.g., Shadden, 2005), and are summarized here. A flow map, F, is defined as a mapping of particles at initial locations x_0 in a fluid to final positions over an interval of time, $t_f - t_0$, using velocity v. The mapping equation is:

$$F_{t_0}^{t_f}\left(x_0\right) = x\left(t_f; x_0, t_0\right) = x_0 + \int_{t_0}^{t_f} v\left(x, t\right) dt \tag{1}$$

The flow map traces each fluid particle from an initial position x_0 at a chosen start time t_0 to a final position x_f at a chosen final time t_f. The flow map can be Taylor expanded about a point x_0 as

$$F_{t_0}^{t_f}\left(x\right) \approx F_{t_0}^{t_f}\left(x_0\right) + \mathbf{J}\left(x - x_0\right) + \ldots \tag{2}$$

where the three dots represent higher-order terms in the Taylor expansion. The Jacobian, **J**, of the flow map is a linearization about x_0, consisting of the matrix of partial derivatives of the final position coordinates with respect to the initial position coordinates. The Jacobian consists of ratios of the final position separation to initial separation of particles infinitesimally near x_0 at time t_0 and thus quantifies the amount of stretching that occurred between t_0 and t_f. In this work, we calculate LCSs in two dimensions (longitude vs. latitude). Future work will calculate LCSs in three dimensions, a more ideal framework for studying the effect of LCSs on vertical transport.

FTLEs are defined as the normalized maximum singular value of the Jacobian matrix of a flow map. An FTLE is computed for every initial particle x_0 in the domain. LCSs are then identified as ridges in FTLE maps. FTLEs have long been used to study mixing at the edge of the polar vortex (Bowman, 1993; Pierce & Fairlie, 1993). LCSs are similar to the popular Lagrangian descriptor "Function M" to define the stratospheric polar vortex edge (e.g., Curbelo et al., 2017; de la Camara et al., 2012; Madrid & Mancho, 2009; Smith & McDonald, 2014). The salient difference between those studies and this work is that they were at stratospheric altitudes, and the focus here is near the mesopause. LCSs have also been identified recently in the thermosphere at midlatitudes, where they act to channel the transport of water vapor plumes associated with space traffic (Wang et al., 2017). Using the same methodologies as Wang et al. (2017), we address whether LCSs reside near the polar winter mesopause and if so, whether they focus the descent of EPP-NO_x into the top of the polar vortex. To accomplish this, we present a case study as a demonstration of the approach and to underpin climatological studies that will be the subject of future work.

This study is structured as follows. Section 2 briefly describes the whole atmosphere model, the trajectory model, and the observations used in this work. Section 3 presents an overview of the meteorology during and after the January 2009 SSW that serves as our case study. Section 4 demonstrates the impact of the split Arctic vortex on the spatial distribution of NO near the mesopause. Section 5 then presents the case study of regionally enhanced NO, bounded horizontally by multiple LCSs, situated above the mesospheric polar vortex. The LCSs are in the vicinity of the trough of a westward traveling 10-day planetary wave (PW). An analysis of vertical transport suggests that descent in the PW trough is five times stronger than at other longitudes. Throughout the study, we make every effort to evaluate the model with observations. Section 6 summarizes the conclusions and gives future directions.

2. Models and Observations

The Whole Atmosphere Community Climate Model with thermosphere-ionosphere eXtension (WACCMX) spans the Earth's surface to ~500 km and simulates relevant processes from the troposphere to the thermosphere and ionosphere (Liu et al., 2010). These include major-species diffusive transport, ion drag, Joule heating, nonlocal thermodynamic equilibrium, and ionospheric physics and chemistry. The WACCMX + DART configuration used here (see Pedatella et al., 2013; Pedatella, Raeder, et al., 2014) employs the Data Assimilation Research Testbed (DART) ensemble adjustment Kalman filter to constrain model meteorology up to ~100 km via data assimilation (Anderson, 2001). For the present study, WACCMX + DART

assimilated conventional meteorological observations (i.e., radiosonde temperature and winds, satellite drift winds, etc.), refractivity from GPS radio occultation in the troposphere and stratosphere, and Sounding of the Atmosphere using Broadband Emission Radiometry (SABER) and Microwave Limb Sounder (MLS) temperature observations from ~20 to ~100 km.

The model spatial resolution is 1.9° × 2.5° horizontally and 1–3.5 km in the vertical. Horizontal winds are output hourly and NO volume mixing ratio (VMR) is output every 6 h. The model incorporates a state-of-the-art gravity wave scheme (Richter et al., 2010) and this is important for MLT dynamics since those altitudes are only constrained by sparse observations. The turbulent Prandtl number that governs thermal diffusion is set to $Pr = 2$ as suggested by Garcia et al. (2014). The Heelis empirical convection pattern (Heelis et al., 1982) is used to account for geomagnetic activity, though geomagnetic activity levels were low during the case study presented here. In the polar MLT, auroral ionization is calculated using the empirical oval of Roble and Ridley (1987), which depends on a specified hemispheric power or geomagnetic K_p index. The model is forced with observed, time-varying values of the solar F10.7 cm radio flux and the K_p index. Neither medium-energy electrons (Pettit et al., 2019) nor D-region ion chemistry (Andersson et al., 2016) is included.

To identify LCSs in WACCMX + DART, hourly model horizontal flow fields at the 0.001 hPa pressure level (near 90 km) are input to the Ionosphere-Thermosphere Algorithm for LCS (ITALCS) trajectory calculation (Wang et al., 2018). An FTLE value is computed at every model longitude and latitude based on 24 h of integration, and these FTLE values are output every 6 h during the month of January 2009. Hourly trajectory positions originating from each model grid point are also archived. Analyses shown here will be limited to the Northern Hemisphere (NH).

A fundamental advantage of using WACCMX + DART flow fields to drive the ITALCS trajectory model is the direct constraint of the MLT region by assimilating SABER and MLS observations. As demonstrated by Pedatella, Raeder, et al. (2014), the assimilation of middle atmosphere temperature observations improves the specification of MLT dynamics even when stratospheric PWs are large. Data assimilation alleviates the climatological mesospheric temperature bias in the model and leads to an improved representation of short-term tidal variability (Pedatella et al., 2016). Also, Siskind et al. (2015) and Pedatella et al. (2018) show that running WACCM and WACCMX with data assimilation in the mesosphere results in more NO descent during February 2009 than running these models without data assimilation, partly correcting the well-known model underestimate noted above.

In this study, we compare model dynamics and chemistry to observations to ensure model fidelity. SABER observations (Russell et al., 1999) are used to evaluate the model geopotential height (GPH) fields. SABER GPH is derived from retrieved temperature and pressure assuming hydrostatic balance (Remsberg et al., 2008). Here, we use version 2.0 temperature data, which have 2 km vertical resolution and precision estimates of less than 4K throughout the mesosphere (García-Comas et al., 2008; Remsberg et al., 2003). Recent comparison of SABER and lidar temperatures shows best agreement between 85 and 95 km (Dawkins et al., 2018), the altitude range of interest here.

We also utilize Atmospheric Chemistry Experiment Fourier Transform Spectrometer (ACE-FTS) (Bernath et al., 2005) and SOFIE (Gordley et al., 2009; Russell et al., 2009) NO VMR measurements to evaluate the model representation of NO. ACE-FTS version 3.5 and SOFIE version 1.3 data have vertical resolutions in the mesosphere of 3–4 km (Boone et al., 2013) and 2 km (Marshall et al., 2011), respectively. ACE-FTS and SOFIE NO data have reported uncertainty estimates of ~80% at 60 km (the highest altitude reported) (Sheese et al., 2016) and 27%–37% at 90 km (Hervig et al., 2019), respectively. Both ACE-FTS and SOFIE sample high northern latitudes (63–71°N) during the case study presented here. Both are solar occultation instruments; and while spatial coverage is sparse, they are well suited to observe zonal asymmetries since they take measurements around a circle of latitude each day.

Since our focus is near 60°N, we leverage hourly Super Dual Auroral Radar Network (SuperDARN, hereafter SD) high-frequency radar measurements of the zonal wind (Hall et al., 1997) to evaluate the model zonal winds near 100 km. During the 2009 case study, there were six operational SD radars spanning approximately 180° of longitude. SD measures the phase shift of meteor echoes to derive the neutral wind velocity carrying the meteor ablation trails. The vertical SD meteor echo distribution extends between 75 and

125 km altitude and is approximately Gaussian, with a mean height of ~100 km altitude and a full width at half maximum of 25–35 km (Chisham & Freeman, 2013; Chisham, 2018). Hourly wind measurements are constructed by least-squares fitting a single horizontal wind vector to hourly binned meteor echo line-of-sight velocities.

To compare SD measurements to the modeled winds, WACCMX-DART winds are first interpolated to an equidistant vertical grid between 75 and 125 km altitude with 2.5 km spacing. The model winds are then vertically averaged with a weighting function representing the SD meteor echo distribution. The vertically averaged winds are sampled at the model gridpoints closest to the locations of operational SD stations. To calculate the temporal evolution of the mean zonal winds at each station, for both the SD observations and model winds, a function representing a mean wind and 24, 12, and 8 h waves are least-squares fitted to the hourly data using a 4-day sliding window following Hibbins and Jarvis (2008) and Hibbins et al. (2011).

Finally, MERRA version 2 reanalysis data (Bosilovich et al., 2015; Molod et al., 2015) are used to define the polar vortex in the stratosphere and mesosphere using the definition described by Harvey et al. (2002). The 6-h instantaneous three-dimensional analyzed meteorological fields in the M2I6NVANA collection are used here (Global Modeling and Assimilation Office, 2015). The data are provided four times daily with a horizontal resolution of 0.5° latitude by 0.625° on 72 model levels that extend from the Earth's surface to 0.015 hPa (~75 km). This reanalysis assimilates MLS temperature and ozone observations above 5 hPa beginning in August 2004 (Gelaro et al., 2017), which constrains the dynamics in the upper stratosphere and lower mesosphere.

3. The 2009 SSW

The January 2009 vortex split SSW has been extensively studied as it remains the strongest and most prolonged SSW in the satellite era (e.g., Coy et al., 2011; Harada et al., 2010; Manney et al., 2009; Schneidereit et al., 2017), and vertical coupling to the thermosphere (e.g., Sassi et al., 2013, 2016) and ionosphere (e.g., Goncharenko, Chau, et al., 2010; Goncharenko, Coster, et al., 2010; Jin et al., 2012; Liu et al., 2011; Pancheva & Mukhtarov, 2012; Pedatella et al., 2016) is apparent during solar minimum. An overview of this event is given in Figure 1 with an emphasis on the MLT. The altitude-time perspective of spatially averaged quantities given in Figures 1a and 1b is often used to visualize the time evolution of SSWs and mesospheric coolings (Labitzke, 1972) as well as the vertical transport of NO. Figures 1a and 1b show that WACCMX + DART reproduces the observed SSW (which began on January 24), in agreement with Pedatella et al. (2018). The model qualitatively reproduces observed features, despite differences in absolute values, for example, in the amplitude of the mesospheric cooling and the temperature of the elevated stratopause. The elevated stratopause is indicative of strong planetary and gravity wave-driven descent in February that resulted in large amounts of NO transported to the stratosphere despite low solar and geomagnetic activity levels (e.g., Randall et al., 2009).

Previous studies of the EPP IE have generally included analyses of NO descent using zonal averages, without regard for spatial inhomogeneities in dynamic or chemical quantities. However, day-to-day wind and NO spatial patterns in the upper mesosphere have not yet been shown. This work fills this gap at the 90 km altitude level and the January 20–30 time period, indicated by the white horizontal lines in Figures 1a and 1b. Since this case study focuses on an altitude and time period following the mesospheric cooling event and preceding the elevated stratopause, there is an intensification in polar descent during the time period analyzed.

Figures 1c and 1d give NH polar maps of GPH at 0.001 hPa (~90 km) on January 23, immediately following the peak stratospheric warming and mesospheric cooling. These maps demonstrate large zonal variability and that SABER (panel c) and the model (panel d) are in agreement with respect to the location of high-pressure and low-pressure systems near the mesopause; both the observations and the model indicate a region of low pressure over the northeast Atlantic and Arctic ocean basins and relatively high pressure over east Asia and the southeast United States. This level of agreement between the model and the observations holds for the duration of this case study. Note, however, since the model assimilates SABER this is not an independent validation. Both the observations and the model indicate maximum zonal GPH variations

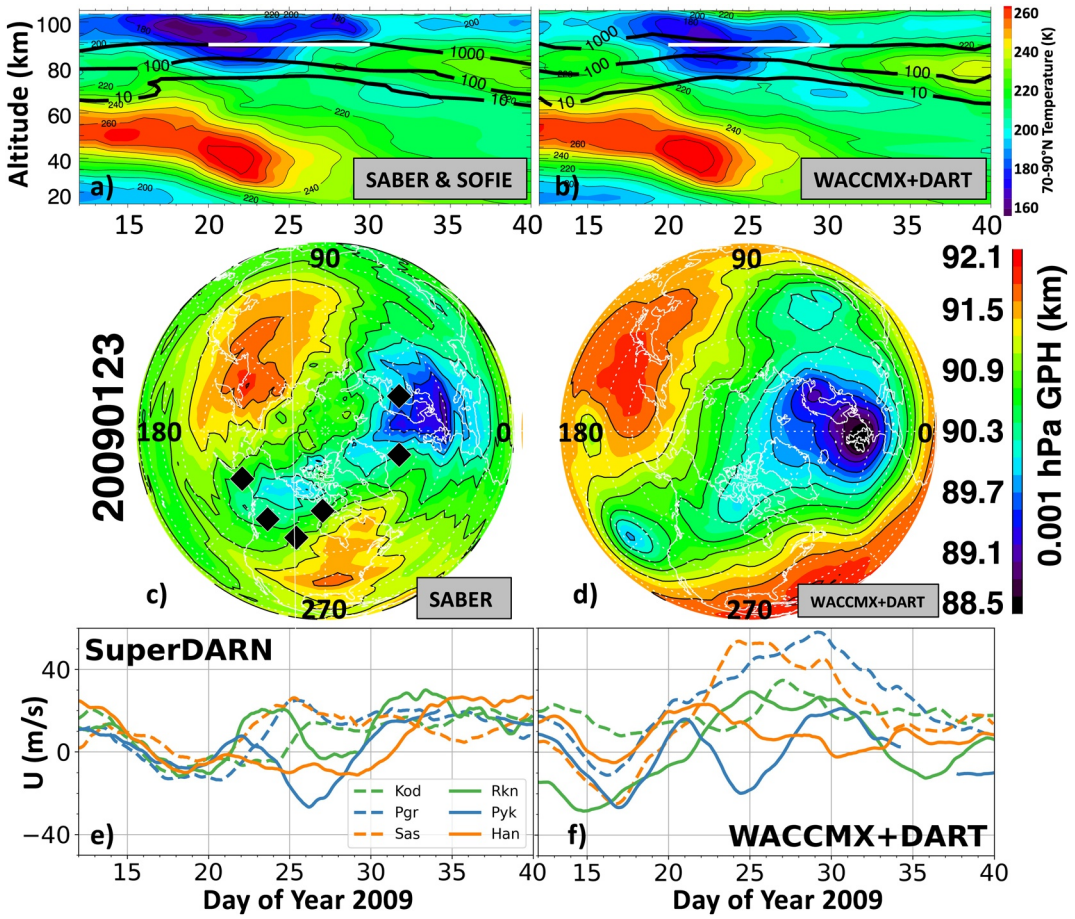

Figure 1. (Top panels) Altitude-time plots of 70°N–90°N average temperature (in color) and zonal mean NO VMR (thick black contours, in ppbv) based on (a) SABER and SOFIE observations and (b) WACCMX + DART from January 12 to February 10, 2009. Major SSW conditions were met on January 24. The NO VMR in panel (b) is the WACCMX + DART values at the SOFIE measurement latitudes. The white horizontal lines at 90 km from January 20 to 30 denote the altitude and time that is the focus of this work. (Middle panels) NH polar plots of daily average GPH in (c) SABER and (d) WACCMX + DART on January 23, 2009 at 0.001 hPa (~90 km). The locations of the six SuperDARN radars operating during this time are indicated by the black diamonds in panel (c). These six radars are, from west to east, in Kodiac Alaska USA (Kod; 57.6°N, 152.2°W), Prince George British Columbia Canada (Pgr; 54°N, 122.6°W), Saskatoon Saskatchewan Canada (Sas; 52.2°N, 106.5°W), Rankin Inlet Nunavut Canada (Rkn; 62.8°N, 92.1°W), Pykkvibaer Iceland (Pyk; 63.8°N, 20.6°W), and Hankasalmi Finland (Han; 62.3°N, 26.6°E). (Bottom panels) time-series of 4-day average zonal winds near 100 km based on (e) SuperDARN and (f) WACCMX + DART. GPH, geopotential height; NH, Northern Hemisphere; SSW, sudden stratospheric warming; VMR, volume mixing ratio.

of 2–3 km in the 50°N–70°N latitude band. This is generally consistent with previously reported large PW amplitudes at this latitude, altitude, and time (Yuan et al., 2012, see their Figure 4).

Comparison of model output to coincident observations with no spatial or temporal averaging is a stringent test of the model. Figures 1e and 1f show SuperDARN radar (panel e) and model (panel f) zonal winds centered on 100 km. This analysis further evaluates the model by comparing with an independent observational source (that was not assimilated). While there are differences between the evolution of the radar versus the model zonal winds at the six radar locations and the amplitudes of the zonal winds are up to a factor of two larger in WACCMX + DART than in observations, the model does simulate a shift from westerly (positive values) to easterly (negative values) zonal winds before the vortex split on January 20 and then a shift back to westerly after the SSW. Further, the model is in excellent agreement with the Pyk radar (solid blue line) over Iceland, which sampled the flow along the poleward flank of the PW trough that we will present in Figure 3. At that location, both the model and the radar indicate a shift from ~10 m s^{-1} westerlies around January 22 to ~20 m s^{-1} easterlies around January 25 and then back to westerlies by the end

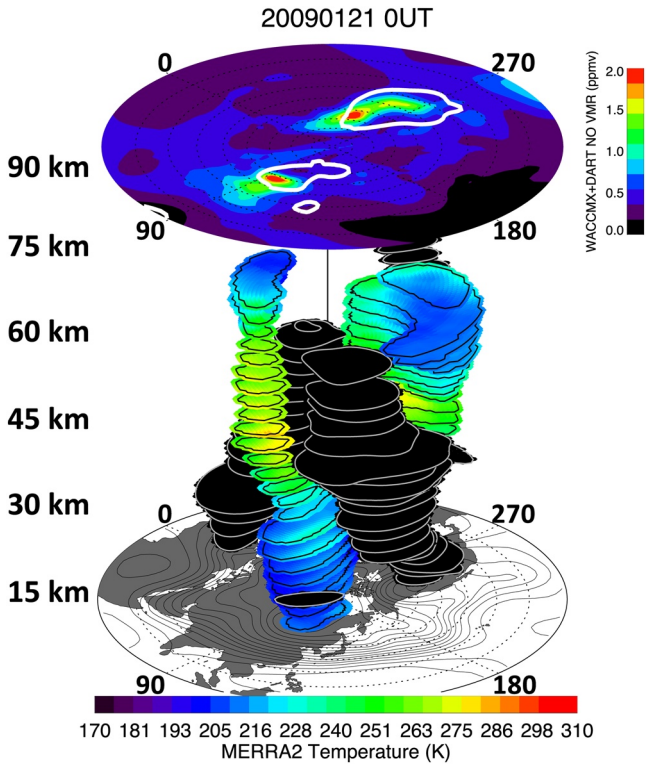

Figure 2. 3-D representation of the Arctic polar vortex (colored by temperature) and stratospheric anticyclones (colored black) on January 21, 2009, at 00 UT based on MERRA-2. An NH polar map of 90 km NO VMR from WACCMX + DART hovers above the split vortex. White contours in the NO map indicate where model GPH deviates by more than 1 km below the zonal mean, indicative of PW troughs. GPH, geopotential height; NH, Northern Hemisphere; PW, planetary wave; VMR, volume mixing ratio.

of the month (note that no Pyk observations are available from 5 UT on Day 34 to 18 UT on Day 37). Overall, Figure 1 is intended to demonstrate that while there are quantitative differences between the model and the observations, there is qualitative agreement in terms of both the zonal mean evolution and the synoptic-scale meteorology in the MLT during this dynamically active time.

4. Imprint of the Split Vortex on NO at the Mesopause

Since WACCMX + DART captures certain key aspects in the MLT for this case, we next show how the split vortex in the stratosphere and mesosphere impacts the NO distribution near the mesopause. Figure 2 illustrates enormous zonal asymmetries that occur throughout the stratosphere and mesosphere on January 21 at 0 UT. At this time the polar vortex (stacked circular regions colored by temperature) is split from 34 to 73 km and there are two vertically deep anticyclones (black circular regions) located over the oceans. SSWs are known to exhibit significant zonal asymmetries due to the large PW structures that drive them (Matsuno, 1970) and zonal averaging obscures these spatial inhomogeneities.

The Arctic polar vortex and anticyclones in Figure 2 are based on MERRA-2 data and are independent of the NO and GPH polar map at 90 km, which is from WACCMX + DART. White contours at 90 km delineate two regions of negative eddy (deviations from the zonal mean) GPH associated with cyclonic flow in the model. These low GPH regions are coincident with the two areas of elevated NO VMR. That the split vortex extends to this altitude was alluded to by Iida et al. (2014), who showed two low MLS GPH regions in polar maps at 90 km on January 19 (2 days earlier). The new result here is that this split circulation resulted in a split distribution of NO. Unfortunately, ACE-FTS and SOFIE measurements (which occurred between 64°N and 69°N on this day) did not intersect the regions of high NO VMR (located between 45°N and 50°N) in the model thus the simulated split NO pattern cannot be confirmed using chemical observations. In the weeks leading up to this split, the modeled NO in the upper mesosphere generally maximized over the pole (not shown). Then, on January 19 at 18 UT both the stratospheric vortex and the GPH and NO fields at 90 km split simultaneously and in similar orientations, with high NO VMR regions in the same longitude sectors as the two polar vortex lobes below. The 90 km NO and eddy GPH fields remained split for 3.5 days (not shown), thus outlasting variability that occurs on diurnal time scales. This result suggests that PW-driven zonal asymmetries in the stratosphere and mesosphere can leave an "imprint" on the NO distribution at the mesopause.

5. Case Study: NO Transport as Evidenced by Lagrangian Coherent Structures

Next, we show the effect of LCSs on the spatial distribution of NO near 90 km on 1 day in WACCMX + DART. Figure 3 gives polar maps on January 26 at 0.001 hPa (near 90 km) to illustrate the horizontal circulation and the spatial patterns in temperature and NO in the wake of the vortex split. Figure 3a shows the GPH near 90 km, similar to Figure 1d but three days later. Also shown here are bold light gray, dark gray, and black contours illustrating the vortex edge location at 30, 50, and 70 km, respectively, which progressively shifts west with increasing altitude. The region of low pressure that resides over the north Atlantic near 90 km is thus seen to be a natural continuation of this westward tilting mesospheric vortex as indicated by the three contour rings (in light gray, dark gray, and black). Horizontal winds flow roughly parallel to both the vortex edge and GPH contours. Vertical continuity in the vortex wind system is consistent with

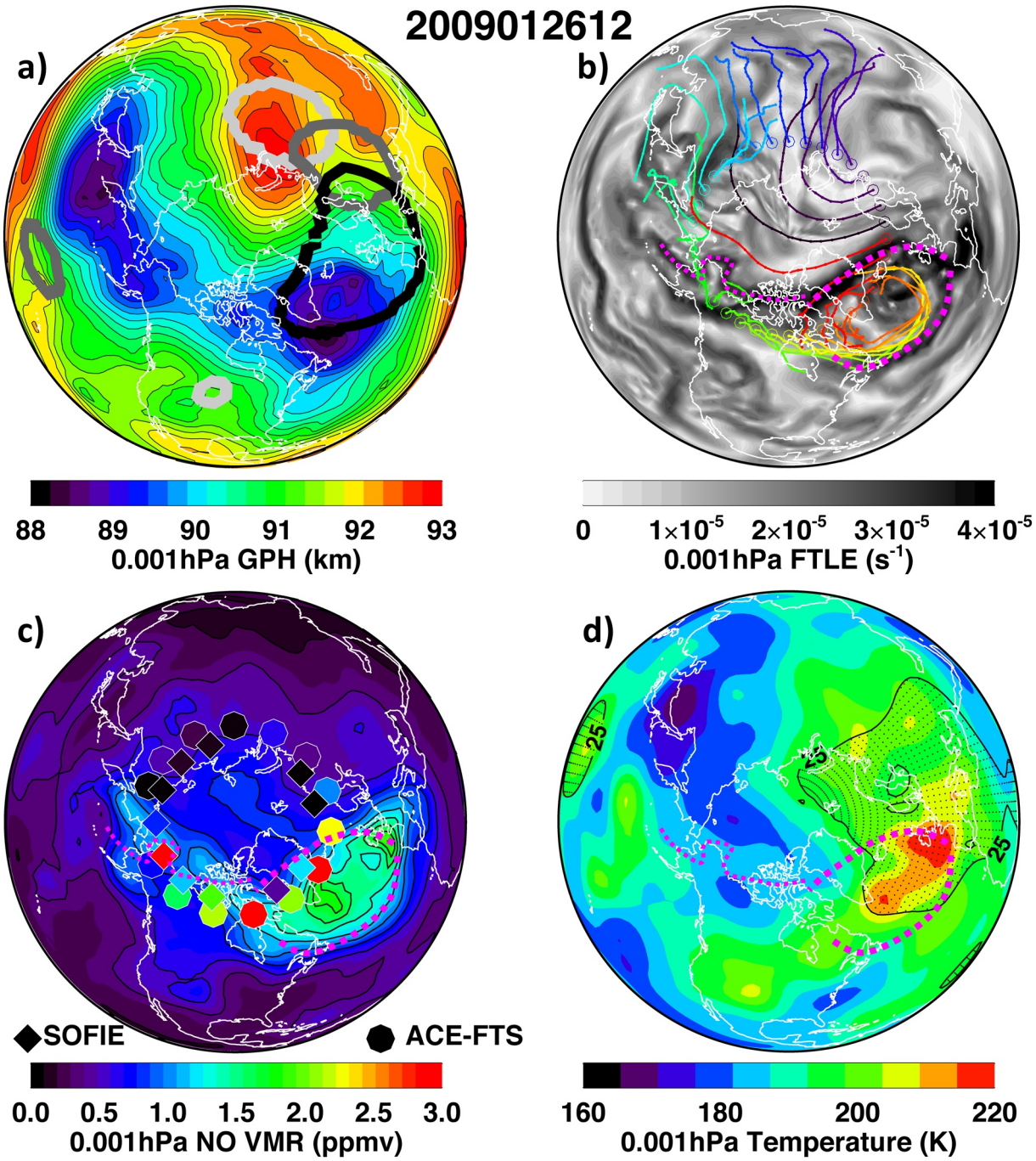

Figure 3. NH polar maps at 0.001 hPa (~90 km) on January 26, 2009 at 12 UT of (a) WACCMX + DART GPH (in color) and MERRA-2 polar vortex edges at 30 km (light gray), 50 km (dark gray), and 70 km (black), (b) simulated FTLE (light and dark gray shading) and 24-h forward trajectory paths (colored lines) for air that originated at the locations given by the open colored circles at 65°N, spaced every 10° in longitude; the pink dotted lines highlight FTLE ridges of interest and these are repeated in panels (c) and (d), (c) NO VMR in WACCMX + DART (color contoured), and NO VMR observed by SOFIE (diamonds) and ACE-FTS (octagons) (note, the ACE-FTS measurement north of Hudson Bay corresponds to a NO VMR of 4.6 ppmv which is outside the color bar range), and (d) WACCMX + DART temperature (in color) with black stippling and boundary lines indicating where the deviation of WACCMX + DART atomic oxygen is at least 25% larger than the zonal mean at each latitude. Both warm temperatures and high atomic oxygen are proxies for descent. FTLE, finite-time Lyapunov exponent; NH, Northern Hemisphere; PW, planetary wave; VMR, volume mixing ratio.

Bhattacharya and Gerrard (2010) who showed mesopause winds to be correlated with stratopause winds when the vortex is displaced from the pole, as it is on this day.

Figure 3b shows the FTLE field (light to dark gray shaded) and 24-h forward trajectories (colored lines) that originated at 65°N, also near 90 km. High FTLE values, or FTLE ridges (dark gray shading), indicate barriers to horizontal transport due to large shear sustained over time. These FTLE ridges are hereafter referred to as LCSs and their spatial distribution reveals the complex nature of the flow field at this altitude and time. The LCSs that are of interest in this work are indicated by the pink dotted lines that trace FTLE ridges located along the poleward, eastern, and equatorward flanks of the north Atlantic low-pressure center shown in Figure 3a. Another LCS of interest extends from western Greenland to Alaska. The concentric trajectory paths inside the low-pressure center over the north Atlantic indicate easterly flow over Iceland, in agreement with observed (SuperDARN radar at Pyk) and modeled zonal winds near 100 km, shown in Figures 1e and 1f. The trajectories illustrate that air inside the north Atlantic low-pressure center remains confined to the 50°N–70°N latitude band (yellow and orange lines), whereas air outside the low (green, blue, and purple lines) is rapidly transported to low latitudes. A well-known property of LCSs is that air parcels on the same side of an LCS experience slow separation for a given amount of time compared to air parcels on opposite sides of an LCS (du Toit & Marsden, 2010). This property has implications for the distribution of NO, in that high latitude air bounded by LCSs is not subject to transport to tropical latitudes. In this case, this sequestration acts to increase the NO chemical lifetime since photolysis rates will tend to be lower between 50°N and 70°N than at low to mid-latitudes. On this day, the latitude distribution of NO lifetime at 0.001 hPa (~90 km) is: 5 days at 20°N, 6 days at 50°N, 10 days at 61°N, 20 days at 67°N, 30 days at 68°N, 40 days at 69°N, and >50 days at 70°N (Brasseur & Solomon, 2005; Minschwaner & Siskind, 1993). Thus, NO contained within a circulation spanning 50°N–70°N will experience more photolysis along the Equatorward flank and negligible photolysis along the poleward flank. If we assume that air spends as much time at 50°N as it does at 70°N, then to first order NO that circulates between 50°N and 70°N will live five times longer ((55 + 6)/2 = ~30 days) than NO that is transported equatorward of 50°N (6 days). These LCSs persist for a week as the low-pressure center migrates to the west, remaining in the 50°N–70°N latitude band; the region occupied by the closed circulation maintains a fairly constant area of ~2 million km^2. The closed circulation persists despite enhancements in the migrating semi-diurnal solar (He et al., 2017) and lunar tides (Chau et al., 2015; Pedatella, Liu, et al., 2014). Even with SSW-induced tidal enhancements, the migrating diurnal and semi-diurnal tidal amplitudes are small (<0.5K) poleward of 40°N at 90 km (Sassi et al., 2013).

Next, we show that the FTLE ridges of interest in Figure 3b are spatially coincident with large horizontal NO gradients in the model, and to a lesser extent in the observations. Figure 3c reveals regionally enhanced model NO over the north Atlantic with maximum mixing ratios located inside the low-pressure center and sharp horizontal gradients coincident with large horizontal gradients in GPH in Figure 3a and the pink dotted lines in Figure 3b. ACE-FTS and SOFIE NO observations are superimposed using filled octagons and diamonds, respectively. Between 50°N and 70°N in the western hemisphere where WACCMX + DART NO VMR values are generally enhanced, the model underestimates observed NO VMR by about a factor of 2, a common trait among models. However, daily average WACCMX + DART NO at the ACE-FTS and SOFIE measurement latitudes is within measurement uncertainties. The observations confirm a distinct PW-1 pattern in NO with high values over the north Atlantic and the Canadian Arctic and generally lower values over Asia. The observations indicate elevated NO VMR values along the extreme poleward flank of the region of enhanced model NO over the north Atlantic. Both the model and the observations also show a tongue of high NO VMR values (>1 ppmv) that extends westward over the Canadian Arctic. These elevated NO values lie along the poleward side of the FTLE ridge that extends to the west from Greenland to Alaska. This westward extension of elevated NO VMR values is likely related to the ongoing westward migration of the entire pattern that will be shown next.

Finally, coincident with the region of high model NO VMR (Figure 3c) are warm model temperatures (Figure 3d) suggestive of adiabatic heating. Temperatures at 60°N, 0.001 hPa over the north Atlantic are 20–40K warmer than at other longitudes around this latitude circle. The black stippled region in Figure 3d is where model atomic oxygen is 25% higher than the zonal mean at each latitude. Atomic oxygen (O) is a dynamical tracer at these altitudes; it has a steep vertical gradient (increasing VMR with increasing altitude) such that high O is a proxy for descent from the lower thermosphere (Smith et al., 2010; Winick et al., 2009). The

model is self-consistent in that regions of high O correspond to regions of warm temperatures, and both suggest descending motion over the north Atlantic. These regional enhancements in the NO and descent would be obscured in zonal averages. Indeed, standard transformed Eulerian mean (TEM) estimates of vertical transport are unable to distinguish variations around a latitude circle.

To summarize, all of the combined aspects presented here paint the following picture: There is a closed circulation coincident with low GPH over the north Atlantic at 90 km with LCSs inhibiting horizontal mixing to the north, east, and south. This circulation (1) contains elevated NO, (2) is associated with enhanced descent, and (3) is the natural upward continuation of the westward tilting polar vortex in the stratosphere and mesosphere. Thus, this meteorological feature provides a transport pathway for air to enter the top of the polar vortex. This is the first work to illustrate the zonally asymmetric nature of NO descent in the polar winter upper mesosphere and couple it to the vortex below.

Next, we examine how the PW patterns in NO and GPH evolve in longitude and time at the ACE-FTS and SOFIE measurement latitudes. Figure 4 gives longitude-time Hovmöller diagrams of NO (color) and eddy GPH (deviation from the zonal mean, contours) at 90 km to illustrate east-west movement of the PW in NO and GPH between 63°N and 71°N latitude during late January 2009. WACCMX + DART NO and eddy GPH are shown in the top row, interpolated to the ACE-FTS (Figure 4a) and SOFIE (Figure 4b) measurement latitudes. ACE-FTS and SOFIE NO observations are shown in panels (c) and (d), respectively, along with eddy GPH from SABER. The latitudes of ACE-FTS and SOFIE measurements are indicated along the right-hand side of each panel and reflect a gradual poleward migration in time of the solar occultations observed by the two satellite instruments. SOFIE maintains about a 5° latitude poleward offset from ACE-FTS, so including both instruments in this analysis provides some indication of the latitude structure. The white and black dashed contours in these plots are positive and negative eddy GPH values, respectively. Hereafter, positive (negative) eddy GPH is referred to as the PW ridge (trough). This figure gives an evaluation of both the model chemistry and dynamics.

During this time period, WACCMX + DART NO VMR is biased 18% lower than measured by ACE-FTS but only 3% lower than measured by SOFIE. However, here the focus is on the longitudinal variability rather than absolute magnitudes, and both the model and the observations show a westward traveling PW-1 pattern in NO and eddy GPH. The PW in SABER eddy GPH peaks on January 24 with amplitudes of 3,096 and 2,723 m at the ACE-FTS and SOFIE measurement latitudes, respectively. This traveling PW is also present at 62.5°N at 80 and 50 km (Iida et al., 2014; see their Figure 6), with maximum amplitudes of 2,200 and 1,400 m, respectively. On January 26, the day shown in Figure 3, highest model NO is in the 270°–360° longitude sector located over the Atlantic. This figure illustrates that this PW-1 pattern then travels westward in time. The westward migration is most evident from January 24 to 29, during which the PW travels ~180° of longitude; thus, it has a period of ~10 days, in agreement with the analysis of MF radar meridional wind data at 69°N and 85 km (Matthias et al., 2012). Such a westward-propagating PW-1 with a period of about 10 days has also been found in WACCM composites (Limpasuvan et al., 2016) and case studies (Orsolini et al., 2017) of other SSW events with elevated stratopauses. In both the model and in the observations, there is coordinated westward movement of high NO in the PW trough (green colors follow the black dashed contours) and extremely low NO remains coincident with the PW ridge (black and purple colors follow the white contours). There are subtle differences between the model and the observations, such as the larger amplitude PW in model GPH (contours, top panels) compared to SABER (contours, bottom panels), and the highest ACE-FTS and SOFIE NO VMRs are not always coincident with the lowest GPH values, as they are in the model. Over this 5-day period, LCS calculations (not shown) indicate that air parcel trajectories that originate inside the PW trough remain confined to the PW trough. These results demonstrate that PWs drive large zonal asymmetries in the distribution of NO near the polar winter mesopause.

6. Descent of NO Enhanced in the PW Trough

Next, we examine model NO VMR within two populations: the PW ridge and the PW trough. This analysis is similar to previous studies that separated trace gas measurements based on whether they were located inside or outside the polar vortex (e.g., Abrams et al., 1996; Lossow et al., 2009; Nassar et al., 2005; Siskind et al., 2000). These studies found distinctly different tracer-tracer relationships and different rates of descent

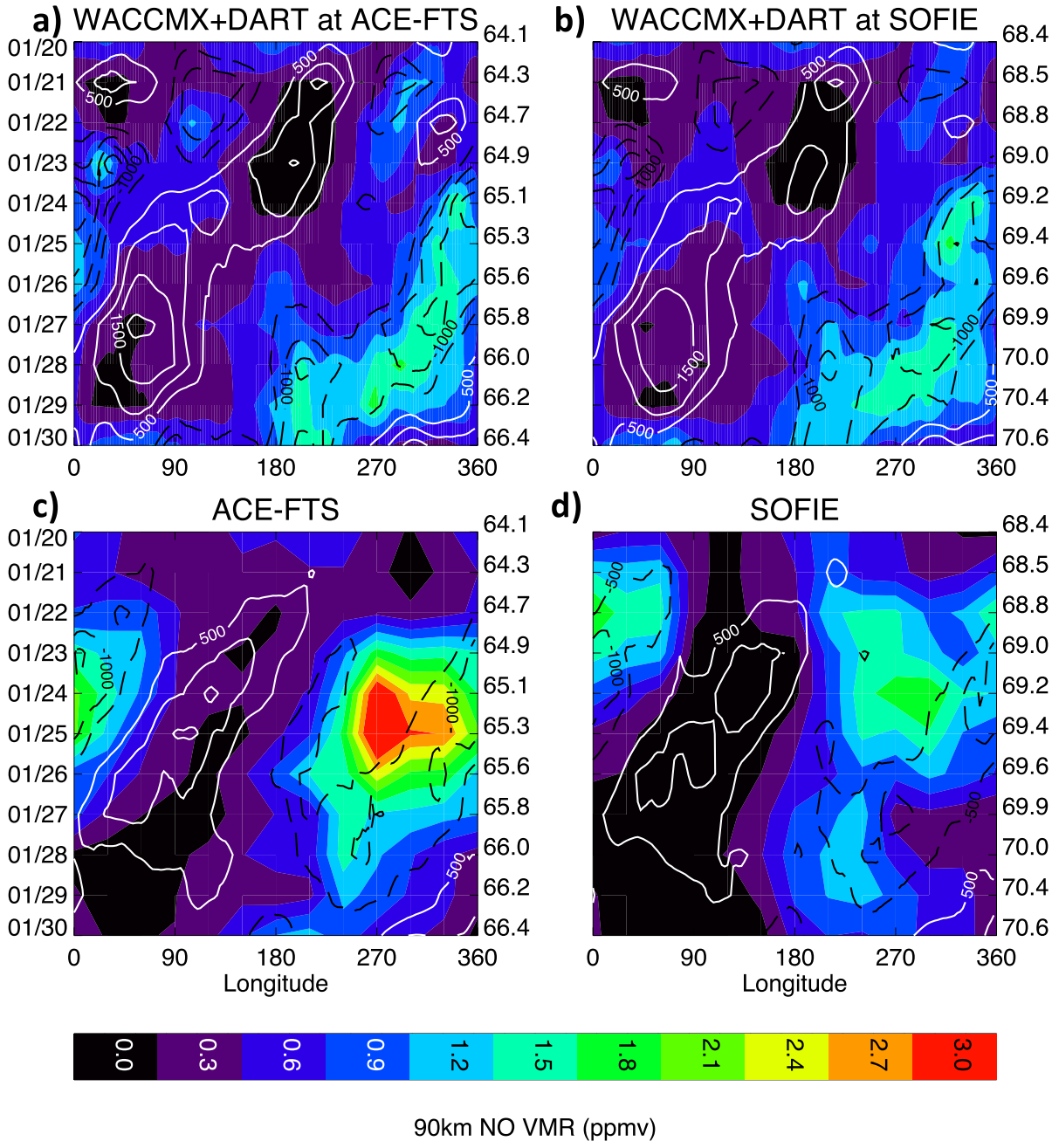

Figure 4. Longitude-time Hovmöller diagrams from January 20 to 30, 2009 of 0.001 hPa NO VMR (in color) and the deviation of GPH from the zonal mean where positive values in white indicate PW ridges and negative values in black dashed indicate PW troughs. GPH data is from WACCMX + DART (top) and SABER (bottom). The top panels show NO VMR in WACCMX + DART at the (a) ACE-FTS and (b) SOFIE measurement latitudes. The bottom panels are NO VMR measured by (c) ACE-FTS and (d) SOFIE. The ACE-FTS and SOFIE measurement latitudes are given along the right side of panels in the left and right columns, respectively. GPH, geopotential height; NH, Northern Hemisphere; PW, planetary wave; VMR, volume mixing ratio.

in different air mass types. The goal here is to determine whether descent rates in the upper mesosphere depend on longitude as defined by PW phase. Thus, on each day from January 24 to 29, we categorize the model grid points (at the SOFIE latitudes shown in Figure 4) by PW phase. One category consists of grid points located in the PW ridge (with positive eddy GPH values) and the other category consists of grid points located in the PW trough (with negative eddy GPH values). On each day we calculate daily mean NO profiles from WACCMX + DART in both air mass types.

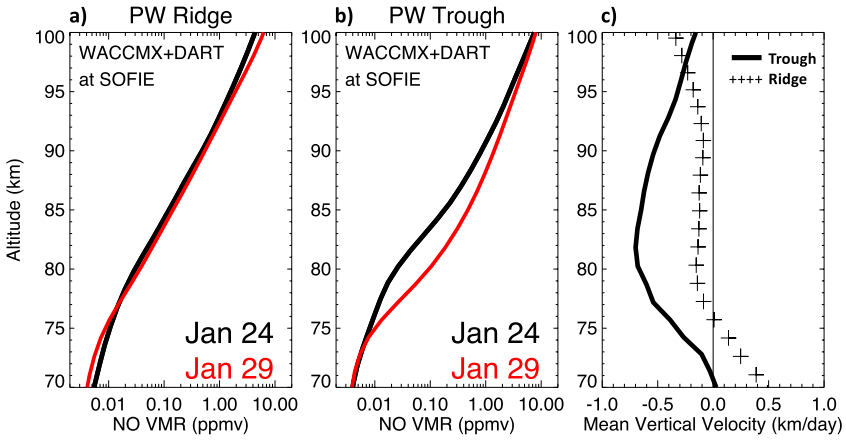

Figure 5. Daily average WACCMX + DART NO VMR profiles on January 24 (black) and January 29 (red) at the SOFIE measurement latitudes and located in the PW (a) ridge and (b) trough. Panel (c) gives vertical profiles of derived vertical velocities in the PW ridge (plus signs) and trough (solid line) of the planetary wave. Negative values indicate descent. PW, planetary wave.

Figure 5a (left panel) shows daily average WACCMX + DART NO profiles on January 24 (black) and January 29 (red) in the PW ridge. Figure 5b shows daily average NO profiles on the same days but in the PW trough. It is clear that there are much larger temporal differences in the NO profiles in the trough than in the ridge. Descent rates are inferred based on the vertical displacement of the NO profiles. This method to infer descent rates has been widely used in previous study (Bailey et al., 2014; Hendrickx et al., 2015; Kvissel et al., 2012; Lee et al., 2011; Siskind et al., 2015; Straub et al., 2012). This technique is valid here since (1) geomagnetic indices are low and we can assume negligible NO production due to particle precipitation; (2) chemical loss of NO is insignificant at latitudes near-polar night, that is, polar NO is mainly controlled by dynamics (Salmi et al., 2011); (3) tidally driven vertical motions are likely negligible given diurnal and semidiurnal migrating tidal amplitudes that are less than 0.5K at 90 km poleward of 40°N (Sassi et al., 2013). Further, Orsolini et al. (2017) demonstrated that the tidal contribution from migrating tides to the vertical component of the residual circulation is small compared to the dominant PW-1 contribution after SSW onset (see their Figure 9).

Figure 5c shows daily average profiles of derived descent rates in the PW ridge and trough. These results indicate that, between 80 and 90 km, the 5-day average descent rate in the PW trough is a factor of 5 stronger than in the PW ridge (−0.64 compared to −0.13 km/day). The same procedure applied to profiles of atomic oxygen (not shown) yields similar results (−0.65 km/day in the trough vs. −0.15 km/day in the ridge). That the derived descent rates based on NO and O profiles are similar lends confidence that they represent the "true" rates of descent (Ryan et al., 2018). These results are consistent with Shepherd et al. (2010) who reported "a dramatic influx of atomic oxygen from the thermosphere" over this same 5-day period at Eureka (80°N, 86°W), which is also located in the PW trough.

In terms of the processes responsible for the descent, Meraner and Schmidt (2016) used HAMMONIA to quantify the role of advective and diffusive processes in the downward transport of NO_x during 2009. They found that large-scale advection is responsible for most of the NO transport from the thermosphere to the mesosphere during this SSW. This is consistent with the results of Smith et al. (2010), who showed that high temperatures coincident with elevated atomic oxygen abundances are indicators of descent driven by large-scale advection. They add that there is also likely a component of the descent driven by molecular diffusion, which is enhanced where it is warmer. Regardless of the driving mechanism(s), we conclude that 83% ($100 \times 0.64/(0.64 + 0.13)$) of all NO descent from 80 to 90 km in late January of 2009 occurred in the longitude sector of the PW trough (assuming from Figure 4 that the ridge and trough occupy comparable areas). This is the case in the model and is confirmed when the ACE-FTS and SOFIE observations are separated in the same way (not shown). Thus, we conclude that zonal asymmetries should be considered when comparing models of NO descent with observations.

7. Conclusions

This work used WACCMX + DART to show that the January 2009 split Arctic vortex in the stratosphere left an imprint on the horizontal distribution of NO at the mesopause. We then presented an 11-day case study in late January during the recovery phase of the 2009 SSW. During the short period of time between the onset of the warming in the stratosphere and the formation of the elevated stratopause around 80–90 km altitude about 10 days later, the reforming mesospheric vortex extends up into the MLT region. The vortex edge in this region is defined not by potential vorticity but by FTLE ridges. We showed for the first time the effects of LCSs on the horizontal transport of NO. We then demonstrate that, near 90 km, LCSs appear in the flow over the north Atlantic in the vicinity of a trough of a westward traveling 10-day PW. This trough is coincident with a region of elevated NO at 90 km, and both the PW trough and elevated NO are located directly above the westward tilting polar vortex in the stratosphere and mesosphere. Because the vortex extends all the way up into the MLT, downward transport from the thermosphere to the upper mesosphere is possible and takes place in this region. Enhanced descent in the PW trough and inhibited horizontal transport of NO by the LCS comprise an efficient transport pathway for air to enter the top of the polar vortex. That is, following the 2009 SSW, air descended over the north Atlantic and Canadian longitude sectors rather than, as is often assumed, descending uniformly in longitude.

New science results are as follows:

1) The split stratospheric polar vortex "imprints" on the spatial distribution of model NO VMR at the mesopause.
2) Elevated NO VMR values in the upper mesosphere remain horizontally confined to high latitudes by LCSs for 11 days.
3) The LCSs occur in the vicinity of the trough of a 10-day westward traveling PW-1.
4) From January 24 to 29, 2009 descent in the upper mesosphere (from ~75 to 95 km) is five times stronger in the longitude sector of the PW trough than in the PW ridge.
5) The descent is likely driven by large-scale vertical advection; that is, most of the residual circulation vertical velocity, a zonally averaged quantity by definition, is focused in the longitude sector of the PW trough.

Future work will quantify how often LCSs coincide with traveling PW troughs at the polar winter mesopause and how often descent depends on PW phase. In particular, this work sets the stage for broader studies that seek to determine whether mesospheric dynamics drive zonal asymmetries in NO descent during more typical polar vortex conditions and in the Southern Hemisphere.

Data Availability Statement

High-end computing resources were provided by NASA to run WACCMX + DART on the Pleiades supercomputer at the NASA Ames research center. Model output for January 20–30, 2009 at 0.001 hPa are provided at https://zenodo.org/record/4563306#.YDhpgeBlDxs. SABER data are available at saber.gats-inc.com. SOFIE data are available at https://spdf.gsfc.nasa.gov/pub/data/aim/sofie/. ACE-FTS data are available at https://databace.scisat.ca/level2/. MERRA-2 data are available at the Data and Information Services Center, managed by the NASA Goddard Earth Sciences (GES) at https://gmao.gsfc.nasa.gov/reanalysis/. The authors acknowledge the use of SuperDARN data. The SuperDARN data are available from Virginia Tech at vt.superdarn.org.

Acknowledgments
V. Lynn Harvey, Seebany Datta-Barua, Nicholas M. Pedatella, and Ningchao Wang acknowledge support from NASA Heliophysics Supporting Research Grant 80NSSC18K1046. V. Lynn Harvey acknowledges partial support from NASA Heliophysics Guest Investigator Grants NNX17AB80G and 80NSSC19K0262. Cora E. Randall acknowledges NSF Grant AGS 1651428. David E. Siskind acknowledges support as a co-investigator of the NASA TIMED/SABER project. Willem E. van Caspel is partly supported by the Research Council of Norway/CoE under contract 22352/F50. These results are partly based upon work supported by the National Center for Atmospheric Research, which is a major facility sponsored by the National Science Foundation under Cooperative Agreement no. 1852977.

References

Abrams, M. C., Manney, G. L., Gunson, M. R., Abbas, M. M., Chang, A. Y., Goldman, A., et al. (1996). Trace gas transport in the Arctic Vortex inferred from ATMOS ATLAS-2 observations during April 1993. *Geophysical Research Letters*, *23*(17), 2345–2348. https://doi.org/10.1029/96GL00704

Anderson, J. L. (2001). An ensemble adjustment Kalman filter for data assimilation. *Monthly Weather Review*, *129*, 2884–2903. https://doi.org/10.1175/1520-0493(2001)129<2884:AEAKFF>2.0.CO;2

Andersson, M. E., Verronen, P. T., Marsh, D. R., Päivärinta, S.-M., & Plane, J. M. C. (2016). WACCM-D-Improved modeling of nitric acid and active chlorine during energetic particle precipitation. *Journal of Geophysical Research - D: Atmospheres*, *121*, 328–410. https://doi.org/10.1002/2015jd024173

Andrews, D. G., Holton, J. R., & Leovy, C. B. (1987). *Middle atmosphere dynamics*. Academic Press.

Bailey, S. M., Thurairajah, B., Randall, C. E., Holt, L., Siskind, D. E., Harvey, V. L., et al. (2014). A multi tracer analysis of thermosphere to stratosphere descent triggered by the 2013 Stratospheric Sudden Warming. *Geophysical Research Letters*, *41*, 5216–5222. https://doi.org/10.1002/2014GL059860

Baldwin, M. P., Ayarzagüena, B., Birner, T., Butchart, N., Butler, A. H., Charlton-Perez, A. J., et al. (2021). Sudden stratospheric warmings. *Reviews of Geophysics*, *59*, e2020RG000708. https://doi.org/10.1029/2020RG000708

Baumgaertner, A. J. G., Seppälä, A., Jöckel, P., & Clilverd, M. A. (2011). Geomagnetic activity related NOx enhancements and polar surface air temperature variability in a chemistry climate model: Modulation of the NAM index. *Atmospheric Chemistry and Physics*, *11*, 4521–4531. https://doi.org/10.5194/acp-11-4521-2011

Bender, S., Sinnhuber, M., Espy, P. J., & Burrows, J. P. (2019). Mesospheric nitric oxide model from SCIAMACHY data. *Atmospheric Chemistry and Physics*, *19*, 2135–2147. https://doi.org/10.5194/acp-19-2135-2019

Bernath, P. F., McElroy, C. T., Abrams, M. C., Boone, C. D., Butler, M., Camy-Peyret, C., & Zou, J. (2005). Atmospheric chemistry experiment (ACE): Mission overview. *Geophysical Research Letters*, *32*, L15S01. https://doi.org/10.1029/2005GL022386

Bhattacharya, Y., & Gerrard, A. J. (2010). Correlations of mesospheric winds with subtle motion of the Arctic polar vortex. *Atmospheric Chemistry and Physics*, *10*, 431–436. https://doi.org/10.5194/acp-10-431-2010

Boone, C. D., Walker, K. A., & Bernath, P. F. (2013). Version 3 retrievals for the Atmospheric Chemistry Experiment Fourier Transform Spectrometer (ACE–FTS). In P. F. Bernath (Ed.), *The atmospheric chemistry experiment ACE at 10: A solar occultation anthology* (pp. 103–127). A. Deepak Publishing.

Bosilovich, M., Akella, S., Coy, L., Cullather, R., Draper, C., Gelaro, R., & Suarez, M. (2015). MERRA-2: Initial Evaluation of the Climate, NASA Tech. Rep. Series on Global Modeling and Data Assimilation. NASA/TM–2015-104606, *43*.

Bowman, K. P. (1993). Large-scale isentropic mixing properties of the Antarctic polar vortex from analyzed winds, *Journal of Geophysical Research*, *98*(D12), 23013–23027, https://doi.org/10.1029/93JD02599

Brasseur, G. P., & Solomon, S. C. (2005). Aeronomy of the middle atmosphere: Chemistry and physics of the stratosphere, in Atmospheric and Oceanographic Sciences Library. Dynamics and transport (3rd ed., Vol. 32, pp. 51–149). Springer.

Butler, A. H., Sjoberg, J. P., Seidel, D. J., & Rosenlof, K. H. (2017). A sudden stratospheric warming compendium. *Earth System Science Data*, *9*, 63–76. https://doi.org/10.5194/essd-9-63-2017

Callaghan, P. F., & Salby, M. L. (2002). Three-dimensionality and forcing of the Brewer-Dobson circulation. *Journal of the Atmospheric Sciences*, *59*, 976–991. https://doi.org/10.1175/1520-0469(2002)059<0976:TDAFOT>2.0.CO;2

Chau, J. L., Hoffmann, P., Pedatella, N. M., Matthias, V., & Stober, G. (2015). Upper mesospheric lunar tides over middle and high latitudes during sudden stratospheric warming events. *Journal of Geophysical Research: Space Physics*, *120*, 3084–3096. https://doi.org/10.1002/2015JA020998

Chisham, G. (2018). Calibrating SuperDARN interferometers using meteor backscatter. *Radio Science*, *53*(6), 761–774. https://doi.org/10.1029/2017rs006492

Chisham, G., & Freeman, M. P. (2013). A reassessment of SuperDARN meteor echoes from the upper mesosphere and lower thermosphere. *Journal of Atmospheric and Solar-Terrestrial Physics*, *102*, 207–221. https://doi.org/10.1016/j.jastp.2013.05.018

Coy, L., Eckermann, S. D., Hoppel, K. W., & Sassi, F. (2011). Mesospheric precursors to the major stratospheric sudden warming of 2009: Validation and dynamical attribution using a ground-to-edge-of-space data assimilation system. *Journal of Advances in Modeling Earth Systems*, *3*, M10002. https://doi.org/10.1029/2011MS000067

Curbelo, J., García-Garrido, V. J., Mechoso, C. R., Mancho, A. M., Wiggins, S., & Niang, C. (2017). Insights into the three-dimensional Lagrangian geometry of the Antarctic polar vortex. *Nonlinear Processes in Geophysics*, *24*, 379–392. https://doi.org/10.5194/npg-24-379-2017

Dawkins, E. C. M., Feofilov, A., Rezac, L., Kutepov, A. A., Janches, D., Höffner, J., et al. (2018). Validation of SABER v2.0 operational temperature data with ground-based lidars in the mesosphere-lower thermosphere region (75-105 km). *Journal of Geophysical Research - D: Atmospheres*, *123*, 9916–9934. https://doi.org/10.1029/2018JD028742

de la Cámara, A., Mancho, A. M., Ide, K., Serrano, E., & Mechoso, C. R. (2012). Routes of transport across the Antarctic polar vortex in the southern spring. *Journal of the Atmospheric Sciences*, *69*(2), 741–752. https://doi.org/10.1175/JAS-D-11-0142.1

Demirhan Bari, D., Gabriel, A., Körnich, H., & Peters, D. W. H. (2013). The effect of zonal asymmetries in the Brewer-Dobson circulation on ozone and water vapor distributions in the northern middle atmosphere. *Journal of Geophysical Research - D: Atmospheres*, *118*, 3447–3466. https://doi.org/10.1029/2012JD017709

du Toit, P. C., & Marsden, J. E. (2010). Horseshoes in hurricanes. *Journal of Fixed Point Theory and Applications*, *7*(2), 351–384. https://doi.org/10.1007/s11784-010-0028-6

Fisher, M., O'Neill, A., & Sutton, R. (1993). Rapid descent of mesospheric air into the stratospheric polar vortex. *Geophysical Research Letters*, *20*(12), 1267–1270. https://doi.org/10.1029/93GL01104

Funke, B., Ball, W., Bender, S., Gardini, A., Harvey, V. L., Lambert, A., et al. (2017). HEPPA-II model-measurement intercomparison project: EPP indirect effects during the dynamically perturbed NH winter 2008-2009. *Atmospheric Chemistry and Physics*, *17*, 3573–3604. https://doi.org/10.5194/acp-17-3573-2017

Garcia, R. R., López-Puertas, M., Funke, B., Marsh, D. R., Kinnison, D. E., Smith, A. K., & González-Galindo, F. (2014). On the distribution of CO_2 and CO in the mesosphere and lower thermosphere. *Journal of Geophysical Research - D: Atmospheres*, *119*, 5700–5718. https://doi.org/10.1002/2013JD021208

Garcia, R. R., Marsh, D. R., Kinnison, D. E., Boville, B. A., & Sassi, F. (2007). Simulation of secular trends in the middle atmosphere, 1950-2003. *Journal of Geophysical Research*, *112*, D09301. https://doi.org/10.1029/2006JD007485

Garcia, R. R. & Solomon, S. (1994). A new numerical model of the middle atmosphere: 2. Ozone and related species. *Journal of Geophysical Research*, *99*, 12937–12951. https://doi.org/10.1029/94JD00725

García-Comas, M., López-Puertas, M., Marshall, B. T., Wintersteiner, P. P., Funke, B., Bermejo-Pantaleón, D., et al. (2008). Errors in Sounding of the Atmosphere using Broadband Emission Radiometry (SABER) kinetic temperature caused by non-local-thermodynamic-equilibrium model parameters. *Journal of Geophysical Research*, *113*, D24106. https://doi.org/10.1029/2008JD010105

Gelaro, R., McCarty, W., Suárez, M. J., Todling, R., Molod, A., Takacs, L., et al. (2017). The modern-era retrospective analysis for research and applications, version 2 (MERRA-2). *Journal of Climate*, *30*, 5419–5454. https://doi.org/10.1175/JCLI-D-16-0758.1

Global Modeling and Assimilation Office. (2015). MERRA-2 inst6_3d_ana_Nv: 3d, 6-hourly, instantaneous, model-level, analysis, analyzed meteorological fields V5.12.4. Goddard Earth Sciences Data and Information Services Center (GES DISC). https://doi.org/10.5067/IUUF4WB9FT4W Accessed 2017.

Goncharenko, L. P., Chau, J. L., Liu, H.-L., & Coster, A. J. (2010). Unexpected connections between the stratosphere and ionosphere. *Geophysical Research Letters*, *37*, L10101. https://doi.org/10.1029/2010GL043125

Goncharenko, L. P., Coster, A. J., Chau, J. L., & Valladares, C. E. (2010). Impact of sudden stratospheric warmings on equatorial ionization anomaly. *Journal of Geophysical Research*, *115*, A00G07. https://doi.org/10.1029/2010JA015400

Gordley, L. L., Hervig, M. E., Fish, C., Russell, J. M. S., III, Cook, J., et al. (2009). The solar occultation for ice experiment. *Journal of Atmospheric and Solar-Terrestrial Physics*, *71*, 300–315. https://doi.org/10.1016/j.jastp.2008.07.012

Hall, G. E., MacDougall, J. W., Moorcroft, D. R., St-Maurice, J. P., Manson, A. H., & Meek, C. E. (1997). Super dual auroral radar network observations of meteor echoes. *Journal of Geophysical Research*, *102*, 14603–14614. https://doi.org/10.1029/97JA00517

Haller, G. (2015). Lagrangian coherent structures. *Annual Review of Fluid Mechanics*, *47*, 137–162. https://doi.org/10.1146/annurev-fluid-010313-141322

Harada, Y., Goto, A., Hasegawa, H., Fujikawa, N., Naoe, H., & Hirooka, T. (2010). A major stratospheric sudden warming event in January 2009. *Journal of the Atmospheric Sciences*, *67*, 2052–2069. https://doi.org/10.1175/2009JAS3320.1

Harvey, V. L., Pierce, R. B., Fairlie, T. D., & Hitchman, M. H. (2002). A climatology of stratospheric polar vortices and anticyclones. *Journal of Geophysical Research*, *107*. https://doi.org/10.1029/2001JD001471

Harvey, V. L., Randall, C. E., Goncharenko, L. P., Becker, E., & France, J. A. (2018). On the upward extension of the polar vortices into the mesosphere. *Journal of Geophysical Research - D: Atmospheres*. 123(17), 9171–9191. https://doi.org/10.1020/2018JD028815

Hauchecorne, A., Bertaux, J.-L., Dalaudier, F., Russell, J. M., III, Mlynczak, M. G., Kyrölä, E., & Fussen, D. (2007). Large increase of NO_2 in the north polar mesosphere in January-February 2004: Evidence of a dynamical origin from GOMOS/ENVISAT and SABER/TIMED data. *Geophysical Research Letters*, *34*, L03810. https://doi.org/10.1029/2006GL027628

He, M., Chau, J. L., Stober, G., Hall, C. M., Tsutsumi, M., & Hoffmann, P. (2017), Application of Manley-Rowe relation in analyzing nonlinear interactions between planetary waves and the solar semidiurnal tide during 2009 Sudden Stratospheric Warming event. *Journal of Geophysical Research: Space Physics*, *122*, 10783–10795, https://doi.org/10.1002/2017JA024630

Heelis, R. A., Lowell, J. K., & Spiro, R. W. (1982). A model of the high-latitude ionospheric convection pattern. *Journal of Geophysical Research*, *87*, 6339–6345. https://doi.org/10.1029/JA087iA08p06339

Hendrickx, K., Megner, L., Gumbel, J., Siskind, D. E., Orsolini, Y. J., Tyssøy, H. N., & Hervig, M. (2015). Observation of 27 day solar cycles in the production and mesospheric descent of EPP-produced NO. *Journal of Geophysical Research: Space Physics*, *120*, 8978–8988. https://doi.org/10.1002/2015JA021441

Hervig, M. E., Marshall, B. T., Bailey, S. M., Siskind, D. E., Russell, III, J. M., III, Bardeen, C. G., et al. (2019). Validation of Solar Occultation for Ice Experiment (SOFIE) nitric oxide measurements. *Atmospheric Measurement Techniques*, *12*, 3111–3121. https://doi.org/10.5194/amt-12-3111-2019

Hibbins, R. E., Freeman, M. P., Milan, S. E., & Ruohoniemi, J. M. (2011). Winds and tides in the mid-latitude Southern Hemisphere upper mesosphere recorded with the Falkland Islands SuperDARN radar. *Annales Geophysicae*, *29*(11), 1985–1996. https://doi.org/10.5194/angeo-29-1985-2011

Hibbins, R. E., & Jarvis, M. J. (2008). A long-term comparison of wind and tide measurements in the upper mesosphere recorded with an imaging Doppler interferometer and SuperDARN radar at Halley, Antarctica. *Atmospheric Chemistry and Physics*, *8*(5), 1367–1376. https://doi.org/10.5194/acp-8-1367-2008

Iida, C., Hirooka, T., & Eguchi, N. (2014). Circulation changes in the stratosphere and mesosphere during the stratospheric sudden warming event in January 2009. *Journal of Geophysical Research - D: Atmospheres*, *119*(12), 7104–7115. https://doi.org/10.1002/2013JD021252

Jin, H., Miyoshi, Y., Pancheva, D., Mukhtarov, P., Fujiwara, H., & Shinagawa, H. (2012). Response of migrating tides to the stratospheric sudden warming in 2009 and their effects on the ionosphere studied by a whole atmosphere-ionosphere model GAIA with COSMIC and TIMED/SABER observations. *Journal of Geophysical Research*, *117*, A10323. https://doi.org/10.1029/2012JA017650

Kinoshita, T., Tomikawa, Y., & Sato, K. (2010). On the three-dimensional residual mean circulation and wave activity flux of the primitive equations. *Journal of the Meteorological Society of Japan*, *88*, 373–394. https://doi.org/10.2151/jmsj.2010-307

Kvissel, O.-K., Orsolini, Y. J., Stordal, F., Limpasuvan, V., Richter, J., & Marsh, D. R. (2012). Mesospheric intrusion and anomalous chemistry during and after a major stratospheric sudden warming. *Journal of Atmospheric and Solar-Terrestrial Physics*, *78–79*, 116–124. https://doi.org/10.1016/j.jastp.2011.08.015

Labitzke, K. (1972). Temperature changes in the mesosphere and stratosphere connected with circulation changes in winter. *Journal of the Atmospheric Sciences*, *29*, 756–766. https://doi.org/10.1175/1520-0469(1972)029<0756:TCITMA>2.0.CO;2

Lee, J. N., Wu, D. L., Manney, G. L., Schwartz, M. J., Lambert, A., Livesey, N. J., et al. (2011). Aura Microwave Limb Sounder observations of the polar middle atmosphere: Dynamics and transport of CO and H_2O. *Journal of Geophysical Research*, *116*, D05110. https://doi.org/10.1029/2010JD014608

Limpasuvan, V., Orsolini, Y. J., Chandran, A., Garcia, R. R., & Smith, A. K. (2016). On the composite response of the MLT to major sudden stratospheric warming events with elevated stratopause. *Journal of Geophysical Research - D: Atmospheres*, *121*, 4518–4537. https://doi.org/10.1002/2015JD024401

Liu, H.-L., Doornbos, E., Yamamoto, M., & Tulasi Ram, S. (2011). Strong thermospheric cooling during the 2009 major stratosphere warming. *Geophysical Research Letters*, *38*, L12102. https://doi.org/10.1029/2011GL047898

Liu, H.-L., Foster, B. T., Hagan, M. E., McInerney, J. M., Maute, A., Qian, L., et al. (2010). Thermosphere extension of the Whole Atmosphere Community Climate Model. *Journal of Geophysical Research*, *115*, A12302. https://doi.org/10.1029/2010JA015586

Lossow, S., Khaplanov, M., Gumbel, J., Stegman, J., Witt, G., Dalin, P., et al. (2009). Middle atmospheric water vapour and dynamics in the vicinity of the polar vortex during the Hygrosonde-2 campaign. *Atmospheric Chemistry and Physics*, *9*, 4407–4417. https://doi.org/10.5194/acp-9-4407-2009

Madrid, J. A. J., & Mancho, A. M. (2009). Distinguished trajectories in time dependent vector fields. *Chaos*, *19*, 013111. https://doi.org/10.1063/1.3056050

Manney, G. L., Schwartz, M. J., Krüger, K., Santee, M. L., Pawson, S., Lee, J. N., et al. (2009). Aura Microwave Limb Sounder observations of dynamics and transport during the record-breaking 2009 Arctic stratospheric major warming. *Geophysical Research Letters*, *36*, L12815. https://doi.org/10.1029/2009GL038586

Manney, G. L., Zurek, R. W., O'Neill, A., & Swinbank, R. (1994). On the motion of air through the stratospheric polar vortex. *Journal of the Atmospheric Sciences*, *51*, 2973–2994. https://doi.org/10.1175/1520-0469(1994)051<2973:OTMOAT>2.0.CO;2

Marshall, B. T., Deaver, L. E., Thompson, R. E., Gordley, L. L., McHugh, M. J., Hervig, M. E., & Russell, J. M., III (2011). Retrieval of temperature and pressure using broadband solar occultation: SOFIE approach and results. *Atmospheric Measurement Techniques*, *4*, 893–907. https://doi.org/10.5194/amt-4-893-2011

Matsuno, T. (1970). Vertical propagation of stationary planetary waves in the winter Northern Hemisphere. *Journal of the Atmospheric Sciences*, *27*(6), 871–883. https://doi.org/10.1175/1520-0469(1970)027<0871:VPOSPW>2.0.CO;2

Matthias, V., Hoffmann, P., Rapp, M., & Baumgarten, G. (2012). Composite analysis of the temporal development of waves in the polar MLT region during stratospheric warmings. *Journal of Atmospheric and Solar-Terrestrial Physics*, *90–91*, 86–96. https://doi.org/10.1016/j.jastp.2012.04.004

McLandress, C., Scinocca, J. F., Shepherd, T. G., Reader, M. C., & Manney, G. L. (2013). Dynamical control of the mesosphere by orographic and nonorographic gravity wave drag during the extended northern winters of 2006 and 2009. *Journal of the Atmospheric Sciences*, *70*(7), 2152–2169. https://doi.org/10.1175/JAS-D-12-0297.1

Meraner, K., & Schmidt, H. (2016). Transport of nitrogen oxides through the winter mesopause in HAMMONIA. *Journal of Geophysical Research - D: Atmospheres*, *121*, 2556–2570. https://doi.org/10.1002/2015JD024136

Meraner, K., Schmidt, H., Manzini, E., Funke, B., & Gardini, A. (2016). Transport of nitrogen oxides through the winter mesopause in HAMMONIA. *Journal of Geophysical Research - D: Atmospheres*, *121*(20), 2556–2570. https://doi.org/10.1002/2015JD024136

Minschwaner, K., & Siskind, D. E. (1993). A new calculation of nitric oxide photolysis in the stratosphere, mesosphere, and lower thermosphere. *Journal of Geophysical Research*, *98*(D11), 20401–20412. https://doi.org/10.1029/93JD02007

Molod, A., Takacs, L., Suarez, M., & Bacmeister, J. (2015). Development of the GEOS-5 atmospheric general circulation model: Evolution from MERRA to MERRA2. *Geoscientific Model Development*, *8*, 1339–1356. https://doi.org/10.5194/gmd-8-1339-2015

Nassar, R., Bernath, P. F., Boone, C. D., Manney, G. L., McLeod, S. D., Rinsland, C. P., et al. (2005). ACE-FTS measurements across the edge of the winter 2004 Arctic vortex. *Geophysical Research Letters*, *32*, L15S05. https://doi.org/10.1029/2005GL022671

Natarajan, M., Remsberg, E. E., Deaver, L. E., & Russell, J. M., III (2004). Anomalously high levels of NOx in the polar upper stratosphere during April, 2004: Photochemical consistency of HALOE observations. *Geophysical Research Letters*, *31*. https://doi.org/10.1029/2004GL020566

Newnham, D. A., Rodger, C. J., Marsh, D. R., Hervig, M. E., & Clilverd, M. A. (2020). Spatial distributions of nitric oxide in the Antarctic wintertime middle atmosphere during geomagnetic storms, *Journal of Geophysical Research: Space Physics*, *125*, e2020JA027846. https://doi.org/10.1029/2020JA027846

Orsolini, Y. J., Limpasuvan, V., Pérot, K., Espy, P., Hibbins, R., Lossow, S., et al. (2017). Modelling the descent of nitric oxide during the elevated stratopause event of January 2013. *Journal of Atmospheric and Solar-Terrestrial Physics*, *155*(2017), 50–61. https://doi.org/10.1016/j.jastp.2017.01.006

Päivärinta, S.-M., Verronen, P. T., Funke, B., Gardini, A., Seppälä, A., & Andersson, M. E. (2016). Transport versus energetic particle precipitation: Northern polar stratospheric NOx and ozone in January-March 2012. *Journal of Geophysical Research - D: Atmospheres*, *121*, 6085–6100. https://doi.org/10.1002/2015JD024217

Pancheva, D., & Mukhtarov, P. (2012). Planetary wave coupling of the atmosphere-ionosphere system during the Northern winter of 2008/2009. *Advances in Space Research*, *50*(9), 1189–1203. https://doi.org/10.1016/j.asr.2012.06.023

Pedatella, N. M., Fang, T.-W., Jin, H., Sassi, F., Schmidt, H., Chau, J. L., et al. (2016). Multimodel comparison of the ionosphere variability during the 2009 sudden stratosphere warming. *Journal of Geophysical Research: Space Physics*, *121*(7), 7204–7225. https://doi.org/10.1002/2016JA022859

Pedatella, N. M., Liu, H.-L., Marsh, D. R., Raeder, K., Anderson, J. L., Chau, J. L., et al. (2018). Analysis and Hindcast experiments of the 2009 Sudden Stratospheric Warming in WACCMX+DART. *Journal of Geophysical Research: Space Physics*, *123*(4), 3131–3153. https://doi.org/10.1002/2017JA025107

Pedatella, N. M., Liu, H.-L., Sassi, F., Lei, J., Chau, J. L., & Zhang, X. (2014). Ionosphere variability during the 2009 SSW: Influence of the lunar semidiurnal tide and mechanisms producing electron density variability. *Journal of Geophysical Research: Space Physics*, *119*, 3828–3843. https://doi.org/10.1002/2014JA019849

Pedatella, N. M., Raeder, K., Anderson, J. L., & Liu, H.-L. (2013). Application of data assimilation in the Whole Atmosphere Community Climate Model to the study of day-to-day variability in the middle and upper atmosphere. *Geophysical Research Letters*, *40*, 4469–4474. https://doi.org/10.1002/grl.50884

Pedatella, N. M., Raeder, K., Anderson, J. L., & Liu, H.-L. (2014). Ensemble data assimilation in the Whole Atmosphere Community Climate Model. *Journal of Geophysical Research - D: Atmospheres*, *119*, 9793–9809. https://doi.org/10.1002/2014JD021776

Pérot, K., & Orsolini, Y. J. (2021). Impact of the major SSWs of February 2018 and January 2019 on the middle atmospheric nitric oxide abundance. *Journal of Atmospheric and Solar-Terrestrial Physics*, *218*, 105586. https://doi.org/10.1016/j.jastp.2021.105586

Pérot, K., Urban, J., & Murtagh, D. P. (2014). Unusually strong nitric oxide descent in the Arctic middle atmosphere in early 2013 as observed by Odin/SMR. *Atmospheric Chemistry and Physics*, *14*(15), 8009–8015. https://doi.org/10.5194/acp-14-8009-2014

Pettit, J. M., Randall, C. E., Peck, E. D., Marsh, D. R., Kamp, M., Fang, X., et al. (2019). Atmospheric effects of >30-kev energetic electron precipitation in the Southern Hemisphere winter during 2003. *Journal of Geophysical Research: Space Physics*, *124*, 8138–8153. https://doi.org/10.1029/2019JA026868

Pierce, R. B., & Fairlie, T. D. A. (1993). Chaotic advection in the stratosphere: Implications for the dispersal of chemically perturbed air from the polar vortex. *Journal of Geophysical Research*, *98*, 18589–18595. https://doi.org/10.1029/93JD01619

Randall, C. E., Harvey, V. L., Holt, L. A., Marsh, D. R., Kinnison, D., Funke, B., & Bernath, P. F. (2015). Simulation of energetic particle precipitation effects during the 2003-2004 Arctic winter. *Journal of Geophysical Research: Space Physics*, *120*, 5035–5048. https://doi.org/10.1002/2015JA021196

Randall, C. E., Harvey, V. L., Manney, G. L., Orsolini, Y., Codrescu, M., Sioris, C., et al. (2005). Stratospheric effects of energetic particle precipitation in 2003-2004. *Geophysical Research Letters*, *32*, L05802. https://doi.org/10.1029/2004GL022003

Randall, C. E., Harvey, V. L., Singleton, C. S., Bailey, S. M., Bernath, P. F., Codrescu, M., et al. (2007). Energetic particle precipitation effects on the Southern Hemisphere stratosphere in 1992-2005. *Journal of Geophysical Research*, *112*, D08308. https://doi.org/10.1029/2006JD007696

Randall, C. E., Harvey, V. L., Singleton, C. S., Bernath, P. F., Boone, C. D., & Kozyra, J. U. (2006). Enhanced NOx in 2006 linked to strong upper stratospheric Arctic vortex. *Geophysical Research Letters*, *33*, L18811. https://doi.org/10.1029/2006GL027160

Randall, C. E., Harvey, V. L., Siskind, D. E., France, J., Bernath, P. F., Boone, C. D., & Walker, K. A. (2009). NOx descent in the Arctic middle atmosphere in early 2009. *Geophysical Research Letters*, *36*, L18811. https://doi.org/10.1029/2009GL039706

Randall, C. E., Rusch, D. W., Bevilacqua, R. M., Hoppel, K. W., & Lumpe, J. D. (1998). Polar Ozone and Aerosol Measurement (POAM) II stratospheric NO_2, 1993-1996. *Journal of Geophysical Research*, *103*, 28361–28371. https://doi.org/10.1029/98JD02092

Reddmann, T., Ruhnke, R., Versick, S., & Kouker, W. (2010). Modeling disturbed stratospheric chemistry during solar-induced NOx enhancements observed with MIPAS/ENVISAT. *Journal of Geophysical Research*, *115*, D00I11. https://doi.org/10.1029/2009JD012569

Remsberg, E., Lingenfelser, G., Harvey, V. L., Grose, W., Russell, J., III, Mlynczak, M., et al. (2003). On the verification of the quality of SABER temperature, geopotential height, and wind fields by comparison with Met Office assimilated analyses. *Journal of Geophysical Research*, *108*. https://doi.org/10.1029/2003JD003720

Remsberg, E. E., Marshall, B. T., García-Comas, M., Krüeger, D., Lingenfelser, G. S., Martin-Torres, J., et al. (2008). Assessment of the quality of the version 1.07 temperature-versus-pressure profiles of the middle atmosphere from TIMED/SABER. *Journal of Geophysical Research*, *113*, D17101. https://doi.org/10.1029/2008JD010013

Richter, J. H., Sassi, F., & Garcia, R. R. (2010). Toward a physically based gravity wave source parameterization in a general circulation model. *Journal of the Atmospheric Sciences*, *67*, 136–156. https://doi.org/10.1175/2009JAS3112.1

Rinsland, C. P., Boone, C., Nassar, R., Walker, K., Bernath, P., McConnell, J. C., & Chiou, L. (2005). Atmospheric Chemistry Experiment (ACE) Arctic stratospheric measurements of NOx during February and March 2004: Impact of intense solar flares. *Geophysical Research Letters*, *32*, L16S05. https://doi.org/10.1029/2005GL022425

Roble, R. G., & Ridley, E. C. (1987). An auroral model for the NCAR thermospheric general circulation model (TGCM). *Annales Geophysicae*, *5A*(6), 369–382.

Rosenfield, J. E., Newman, P. A., & Schoeberl, M. R. (1994). Computations of diabatic descent in the stratospheric polar vortex. *Journal of Geophysical Research*, *99*(D8), 16677–16689. https://doi.org/10.1029/94JD01156

Russell, J. M., III, Bailey, S. M., Gordley, L. L., Rusch, D. W., Horányi, M., Hervig, M. E., et al. (2009). The Aeronomy of Ice in the Mesosphere (AIM) mission: Overview and early science results. *Journal of Atmospheric and Solar-Terrestrial Physics*, *71*, 289–299. https://doi.org/10.1016/j.jastp.2008.08.011

Russell, J. M., III, Mlynczak, M. G., Gordley, L. L., Tansock, J., & Esplin, R. (1999). Overview of the SABER experiment and preliminary calibration results. *Proceedings of SPIE-The International Society for Optical Engineering*, *3756*, 277–288. https://doi.org/10.1117/12.366382

Ryan, N. J., Kinnison, D. E., Garcia, R. R., Hoffmann, C. G., Palm, M., Raffalski, U., & Notholt, J. (2018). Assessing the ability to derive rates of polar middle-atmospheric descent using trace gas measurements from remote sensors. *Atmospheric Chemistry and Physics*, *18*, 1457–1474. https://doi.org/10.5194/acp-18-1457-2018

Salmi, S.-M., Verronen, P. T., Thölix, L., Kyrölä, E., Backman, L., Karpechko, A. Y., & Seppälä, A. (2011). Mesosphere-to-stratosphere descent of odd nitrogen in February-March 2009 after sudden stratospheric warming. *Atmospheric Chemistry and Physics*, *11*, 4645–4655. https://doi.org/10.5194/acp-11-4645-2011

Sassi, F., Liu, H. L., & Emmert, J. T. (2016). Traveling planetary-scale waves in the lower thermosphere: Effects on neutral density and composition during solar minimum conditions. *Journal of Geophysical Research: Space Physics*, *121*, 1780–1801. https://doi.org/10.1002/2015JA022082

Sassi, F., Liu, H.-L., Ma, J., & Garcia, R. R. (2013). The lower thermosphere during the northern hemisphere winter of 2009: A modeling study using high-altitude data assimilation products in WACCM-X. *Journal of Geophysical Research - D: Atmospheres*, *118*, 8954–8968. https://doi.org/10.1002/jgrd.50632

Scherhag, R. (1952). Die explosionsartigen Stratosphärenerwärmungen des Spätwinters 1951/52. *Berichte des deutschen Wetterdienstes in der US-Zone*, *6*(38), 51–63.

Schneidereit, A., Peters, D. H. W., Grams, C. M., Quinting, J. F., Keller, J. H., Wolf, G., et al. (2017). Enhanced tropospheric wave forcing of two anticyclones in the prephase of the January 2009 major stratospheric sudden warming event. *Monthly Weather Review*, *145*(5), 1797–1815. https://doi.org/10.1175/MWR-D-16-0242.1

Schoeberl, M. R., Lait, L. R., Newman, P. A., & Rosenfield, J. E. (1992). The structure of the polar vortex. *Journal of Geophysical Research*, *97*, 7859–7882. https://doi.org/10.1029/91JD02168

Shadden, S. C., Lekien, F., & Marsden, J. E. (2005). Definition and properties of Lagrangian coherent structures from finite-time Lyapunov exponents in two-dimensional aperiodic flows. *Physica D: Nonlinear Phenomena*, *212*(3–4), 271–304. https://doi.org/10.1016/j.physd.2005.10.007

Sheese, P. E., Strong, K., Gattinger, R. L., Llewellyn, E. J., Urban, J., Boone, C. D., & Smith, A. K. (2013). Odin observations of Antarctic nighttime NO densities in the mesosphere-lower thermosphere and observations of a lower NO layer. *Journal of Geophysical Research - D: Atmospheres*, *118*, 7414–7425. https://doi.org/10.1002/jgrd.505610.1002/jgrd.50563

Sheese, P. E., Walker, K. A., Boone, C. D., McLinden, C. A., Bernath, P. F., Bourassa, A. E., et al. (2016). Validation of ACE-FTS version 3.5 NOy species profiles using correlative satellite measurements. *Atmospheric Measurement Techniques*, *9*, 5781–5810. https://doi.org/10.5194/amt-9-5781-2016

Shepherd, M. G., Cho, Y.-M., Shepherd, G. G., Ward, W., & Drummond, J. R. (2010). Mesospheric temperature and atomic oxygen response during the January 2009 major stratospheric warming. *Journal of Geophysical Research*, *115*, A07318. https://doi.org/10.1029/2009JA015172

Sinnhuber, M., Berger, U., Funke, B., Nieder, H., Reddmann, T., Stiller, G., et al. (2018). NOy production, ozone loss and changes in net radiative heating due to energetic particle precipitation in 2002-2010. *Atmospheric Chemistry and Physics*, *18*, 1115–1147. https://doi.org/10.5194/acp-18-1115-2018

Siskind, D. E., Bacmeister, J. T., Summers, M. E., & Russell, J. M., III (1997). Two-dimensional model calculations of nitric oxide transport in the middle atmosphere and comparison with Halogen Occultation Experiment data. *Journal of Geophysical Research*, *102*, 3527–3545. https://doi.org/10.1029/96JD02970

Siskind, D. E., Eckermann, S. D., McCormack, J. P., Coy, L., Hoppel, K. W., & Baker, N. L. (2010). Case studies of the mesospheric response to recent minor, major, and extended stratospheric warmings. *Journal of Geophysical Research*, *115*, D00N03. https://doi.org/10.1029/2010JD014114

Siskind, D. E., Harvey, V. L., Sassi, F., McCormack, J. P., Randall, C. E., Hervig, M. E., & Bailey, S. M. (2021). 2- and 3-dimensional structure of the descent of mesospheric trace constituents after the 2013 SSW elevated stratopause event. *Atmospheric Chemistry and Physics Discuss*. https://doi.org/10.5194/acp-2021-68,2021

Siskind, D. E., Nedoluha, G. E., Randall, C. E., Fromm, M., & Russell, J. M., III (2000). An assessment of southern hemisphere stratospheric NOx enhancements due to transport from the upper atmosphere. *Geophysical Research Letters*, *27*, 329–332. https://doi.org/10.1029/1999GL010940

Siskind, D. E., Sassi, F., Randall, C. E., Harvey, V. L., Hervig, M. E., & Bailey, S. M. (2015). Is a high-altitude meteorological analysis necessary to simulate thermosphere-stratosphere coupling? *Geophysical Research Letters*, *42*, 8225–8230. https://doi.org/10.1002/2015GL065838

Smith, A. K. (2012). Global dynamics of the MLT. *Surveys in Geophysics*, *33*, 1177–1230. https://doi.org/10.1007/s10712-012-9196-9

Smith, A. K., Garcia, R. R., Marsh, D. R., & Richter, J. H. (2011). WACCM simulations of the mean circulation and trace species transport in the winter mesosphere. *Journal of Geophysical Research*, *116*, D20115. https://doi.org/10.1029/2011JD016083

Smith, A. K., Marsh, D. R., Mlynczak, M. G., & Mast, J. C. (2010). Temporal variations of atomic oxygen in the upper mesosphere from SABER. *Journal of Geophysical Research*, *115*, D18309. https://doi.org/10.1029/2009JD013434

Smith, M. L., & McDonald, A. J. (2014). A quantitative measure of polar vortex strength using the function M. *Journal of Geophysical Research - D: Atmospheres*, *119*, 5966–5985. https://doi.org/10.1002/2013JD020572

Smith-Johnsen, C., Marsh, D. R., Orsolini, Y., Nesse Tyssøy, H., Hendrickx, K., Sandanger, M. I., et al. (2018). Nitric oxide response to the April 2010 electron precipitation event: Using WACCM and WACCM-D with and without medium-energy electrons. *Journal of Geophysical Research: Space Physics*, *123*, 5232–5245. https://doi.org/10.1029/2018JA025418

Straub, C., Tschanz, B., Hocke, K., Kämpfer, N., & Smith, A. K. (2012). Transport of mesospheric H_2O during and after the stratospheric sudden warming of January 2010: Observation and simulation. *Atmospheric Chemistry and Physics*, *12*, 5413–5427. https://doi.org/10.5194/acp-12-5413-2012

Wang, N., Datta-Barua, S., Chartier, A. T., Ramirez, U., & Mitchell, C. N. (2018). Horseshoes in the high-latitude ionosphere. *Journal of Geophysical Research: Space Physics*, *123*(7), 5831–5849. https://doi.org/10.1029/2017JA025077

Wang, N., Ramirez, U., Flores, F., & Datta-Barua, S. (2017). Lagrangian coherent structures in the thermosphere: Predictive transport barriers. *Geophysical Research Letters*, *44*, 4549–4557. https://doi.org/10.1002/2017GL072568

Winick, J. R., Wintersteiner, P. P., Picard, R. H., Esplin, D., Mlynczak, M. G., Russell, J. M., III, & Gordley, L. L. (2009). OH layer characteristics during unusual boreal winters of 2004 and 2006. *Journal of Geophysical Research*, *114*, A02303. https://doi.org/10.1029/2008JA013688

Yuan, T., Thurairajah, B., She, C.-Y., Chandran, A., Collins, R. L., & Krueger, D. A. (2012). Wind and temperature response of midlatitude mesopause region to the 2009 Sudden Stratospheric Warming. *Journal of Geophysical Research*, *117*, D09114. https://doi.org/10.1029/2011JD017142